Research Article

Nano Research
2024, 17(3): 1676–1686

ISSN 1998-0124 CN 11-5974/O4
https://doi.org/10.1007/s12274-023-6198-5

Enhanced electromagnetic wave absorption via optical fiber-like PMMA@$Ti_3C_2T_x$@SiO_2 composites with improved impedance matching

Huanhuan Niu[1,2], Xuewen Jiang[1], Wei Li[3] (✉), Zhiyu Min[4], Budi Riza Putra[5], Wulan Tri Wahyuni[6], Hailong Wang[1], Rui Zhang[1,4], and Bingbing Fan[1] (✉)

[1] *School of Material Science and Engineering, Zhengzhou University, Zhengzhou 450001, China*
[2] *School of Materials Science and Engineering, Tongji University, Shanghai 201804, China*
[3] *Department of Materials and Earth Sciences, Technical University of Darmstadt, Darmstadt 64287, Germany*
[4] *School of Material Science and Engineering, Luoyang Institute of Science and Technology, Luoyang 471023, China*
[5] *Research Center for Metallurgy, National Research and Innovation Agency (BRIN), PUSPIPTEK Gd. 470, South Tangerang, Banten 15315, Indonesia*
[6] *Analytical Chemistry Division, Department of Chemistry, Faculty of Mathematics and Natural Sciences, IPB University, West Java 16680, Indonesia*

Received: 24 August 2023 / **Revised:** 10 September 2023 / **Accepted:** 12 September 2023

ABSTRACT

$Ti_3C_2T_x$ nanosheets have attracted significant attention for their potential in electromagnetic wave absorption (EWA). However, their inherent self-stacking and exorbitant electrical conductivity inevitably lead to serious impedance mismatch, restricting their EWA application. Therefore, the optimization of impedance matching becomes crucial. In this work, we developed polymethyl methacrylate (PMMA)@$Ti_3C_2T_x$@SiO_2 composites with a sandwich-like core–shell structure by coating SiO_2 on PMMA@$Ti_3C_2T_x$. The results demonstrate that the superiority of the SiO_2 layer in combination with PMMA@$Ti_3C_2T_x$, outperforming other relative graded distribution structures and meeting the requirements of EWA equipment. The resulting PMMA@$Ti_3C_2T_x$@SiO_2 composites achieved a minimum reflection loss of −58.08 dB with a thickness of 1.9 mm, and an effective absorption bandwidth of 2.88 GHz. Mechanism analysis revealed that the structural design of SiO_2 layer not only optimized impedance matching, but also synergistically enhanced multiple loss mechanisms such as interfacial polarization and dipolar polarization. Therefore, this work provides valuable insights for the future preparation of high-performance electromagnetic wave absorbing $Ti_3C_2T_x$-based composites.

KEYWORDS

polymethyl methacrylate (PMMA)@$Ti_3C_2T_x$@SiO_2 composites, impedance match, SiO_2 layer, optical fiber-like structure, interfacial polarization and dipolar polarization.

1 Introduction

$Ti_3C_2T_x$ nanosheets, classified as two-dimensional (2D) material, have garnered widespread due to their intrinsic conductivity, large specific surface area and rich surface functional groups and defects, making them highly promising for new-generation high-efficiency electromagnetic wave absorption (EWA) applications [1–4]. However, the excessive permittivity and self-stacking of $Ti_3C_2T_x$ nanosheets lead to impedance mismatch, limiting their practical use as high-performance absorbers in civilian fields.

To overcome this challenge and advance towards practical applications, researchers have focused on the combination and structural design of $Ti_3C_2T_x$ nanosheets. Various approaches, such as porous structures [5–8], heterostructures [9, 10], hollow structures [11], and the doping of magnetic [12–14], dielectric [15–17], and other materials have been explored. Controllable structure and precise combination of $Ti_3C_2T_x$ nanosheets remain major challenges, despite significant progress.

The design of core–shell structure has been proved to be an effective way for introducing heterointerface and thereby enhancing EWA performance of $Ti_3C_2T_x$ nanosheet [18–20]. However, the exposure of more oxidizable surfaces in the core–shell structure can lead to the preferential oxidation of $Ti_3C_2T_x$ nanosheets. Even when protected by inert gas, oxidation reactions remain unavoidable. Existing core–shell structures, such as CoNi@C [21], Co@C [22], CoNi@$Ti_3C_2T_x$ [23], have achieved a highly effective electromagnetic wave absorption capability. However, the use of magnetic metals, which are predominantly comprised of heavy metal elements, fails to meet the requirements for lightweight electromagnetic wave absorption materials.

In contrast, polymethyl methacrylate (PMMA) offers distinct advantages, such as lightweight, low cost and ease of combination with $Ti_3C_2T_x$ nanosheets [24]. Therefore, the PMMA@$Ti_3C_2T_x$ core–shell structure, utilizing PMMA as a template, presents a promising solution to fulfill the lightweight requirements of EWA materials. However, the weak antioxidation ability of $Ti_3C_2T_x$ remains a challenging issue that needs to be addressed to fully meet the lightweighting demands of EWA materials.

Address correspondence to Wei Li, wei.li@mr.tu-darmstadt.de; Bingbing Fan, fanbingbing@zzu.edu.cn

SiO_2 has been identified as a candidate for microwave transparent materials due to its advantageous properties, such as low density, high-temperature resistance, exceptional strength, Moreover, SiO_2's ability to generate interfacial barrier effects, which effectively improves dielectric loss during microwave absorption processes, further enhances its appeal as an attractive option for developing efficient microwave absorption materials [25]. In addition, the optical fiber-like structure is constructed by SiO_2 and $Ti_3C_2T_x$. Compared with SiO_2, $Ti_3C_2T_x$ with higher dielectric parameters is equivalent to the fiber core, and SiO_2 is regarded as the cladding. The electromagnetic wave will be fully reflected after entering the absorber, thus achieving more efficient electromagnetic wave absorption. Owing to the existence of SiO_2 and unique structure, the designed CoNi@Air@C/SiO_2@PPy MCNCs presented excellent comprehensive EWA performances in terms of low RL and large effective absorption bandwidth (EAB) [26].

Additionally, coating $Ti_3C_2T_x$ with SiO_2 effectively protects $Ti_3C_2T_x$ from oxidation, further enhancing their stability and performance in EMA applications. The heterogeneous interfaces generated between $Ti_3C_2T_x$ and SiO_2 cannot only increase the interface polarization, but also prolong the propagation path of electromagnetic waves. In addition, the SiO_2 coating on the surface acts as an impedance match layer to reduce the dielectric constant contrast between free space and the $Ti_3C_2T_x$ nanosheet, thereby inducing more electromagnetic waves (EW) to enter the interior of the material for subsequent attenuation loss.

In this study, we have devised a straightforward approach to fabricate optical fiber-like PMMA@$Ti_3C_2T_x$@SiO_2 composites with a unique sandwich-like core–shell structure. The method involves utilizing PMMA as a template and employing the sol-gel method. The $Ti_3C_2T_x$ nanosheets are securely wrapped around the PMMA template through hydrogen bonding. Subsequently, a SiO_2 layer is coated onto the surface of $Ti_3C_2T_x$ nanosheets using the sol-gel method, resulting in the formation of numerous heterointerfaces. The PMMA@$Ti_3C_2T_x$@SiO_2 composites attained a minimum reflection loss value of −58.08 dB with a thickness of 1.9 mm and an EAB of 2.88 GHz. The method proposed in this work provides a guideline for the future preparation of $Ti_3C_2T_x$-based composites with high-performance electromagnetic wave absorption.

2 Experimental

2.1 Raw materials

The precursor particles of Ti_3AlC_2 with a particle size of 400 mesh were purchased from Jilin 11 Technology Co., Ltd., China. Anhydrous ethanol (99.7%) and hydrochloric acid (HCl, 36% to 38%) were commercially obtained from Luoyang Chemical Tiancheng Reagent Co., Ltd., China. PMMA and lithium fluoride (LiF, ≥ 99%) were acquired from Shanghai Macklin Biochemical Co., Ltd. Ethyl orthosilicate (TEOS, Tianjin Kemer Chemical Reagent Co., Ltd.) and ammonia (analytical purity, Guangdong Xilong Technology Co., Ltd.) also used in this work.

2.2 Preparation of PMMA@$Ti_3C_2T_x$@SiO_2 with sandwich-like core–shell structure

$Ti_3C_2T_x$ nanosheet was prepared by chemical etching of Ti_3AlC_2 precursor, and the detailed synthesis procedures can be referred to in our previous work [27]. For the fabrication of sandwich-like core–shell structured PMMA@$Ti_3C_2T_x$@SiO_2 composites, we employed hydrogen bonding and the sol-gel method. Homogeneous PMMA microspheres, with an approximate size of ~ 1.8 μm, served as the template core.

Firstly, a mixture of 0.2 g PMMA microspheres and 5 mL anhydrous ethanol underwent sonication for 5–10 min. Subsequently, 30 mL of $Ti_3C_2T_x$ nanosheet solution (1.6 mg/mL) was added to the obtained mixture. The hybrid materials were continuously stirred for 1 h, and then the resulting mixture was transferred to a centrifugal tube and centrifuged at 8000 r/min for 10 min to collect sediment, which is the PMMA@$Ti_3C_2T_x$ composites.

The initially obtained PMMA@$Ti_3C_2T_x$ was dispersed in 400 mL of an aqueous ethanol solution (deionized water:ethanol = 1:4) and stirred for 10 min to ensure uniform dispersion. Subsequently, a mixture containing 7 mL of $NH_4(OH)$ and 2 mL TEOS was added. The resulting solution was magnetically stirred for 20 h at 25 °C, followed by a 10 min standing period to allow the white suspension to settle. The supernatant was then poured off, and the remaining precipitate was collected using centrifugation. Afterward, the precipitate was washed four times, alternately with deionized water and ethanol. Finally, the washed precipitate was vacuum dried for 6 h at 60 °C to obtain the PMMA@$Ti_3C_2T_x$@SiO_2 composites.

In order to investigate the impact of SiO_2 layer on impedance match, PMMA@$Ti_3C_2T_x$@SiO_2 (PTS) composites with different TEOS contents were prepared using the same synthesis process described above. The resulting products were labeled as PTS-1, PTS-2, PTS-3 and PTS-4, corresponding to the TEOS contents of 2, 3, 4 and 5 mL, respectively.

2.3 Characterization

The phase composition of PMMA@$Ti_3C_2T_x$@SiO_2 composites were determined by X-ray diffractometer (XRD; Cu Kα radiation, Empyrean X, PAN alytical B.V., Holland). The morphology of the samples was investigated using scanning electron microscope (SEM; JSM-7001F, JEOL, Tokyo, Japan). Furthermore, a transmission electron microscope (TEM; JEM-2100f, JEOL, Tokyo, Japan) coupled with an energy-dispersive X-ray spectroscope was used to examine intricate microstructure and charge distribution of the specimens.

The X-ray photoelectron spectroscope (XPS; Thermo Fisher Scientific, K-alpha, Waltham, MA, USA) was utilized to examine the surface elemental composition and chemical bonding of the composites. The synchronous thermal analyzer (TA449F3, NETZSCH, Germany) was used to characterize the high temperature oxidation state of PMMA@$Ti_3C_2T_x$@SiO_2 composites. Micro-infrared spectroscopy was used to characterize the presence of hydrogen bonds.

For the characterization of effective EWA, the PMMA@$Ti_3C_2T_x$@SiO_2 composites (50 wt.%) were uniformly mixed with paraffin (50 wt.%), and then pressed into a coaxial ring with an outer diameter of 7.00 mm and an inner diameter of 3.04 mm. The complicated permittivity and permeability of the samples were measured in the frequency range of 2–18 GHz using a coaxial technique and a vector network analyzer (MS46322B) from Anli Co., Ltd. (Japan).

3 Results and discussion

3.1 Phase composition and microstructure

Figure 1 depicts the step-by-step preparation process of the PMMA@$Ti_3C_2T_x$. Succinctly, PMMA@$Ti_3C_2T_x$ was prepared through the hydrogen bond interaction between PMMA and $Ti_3C_2T_x$. Subsequently, PMMA@$Ti_3C_2T_x$ was employed as a substrate for the deposition of SiO_2, prepared via the sol-gel method, resulting in the formation of PMMA@$Ti_3C_2T_x$@SiO_2 composites.

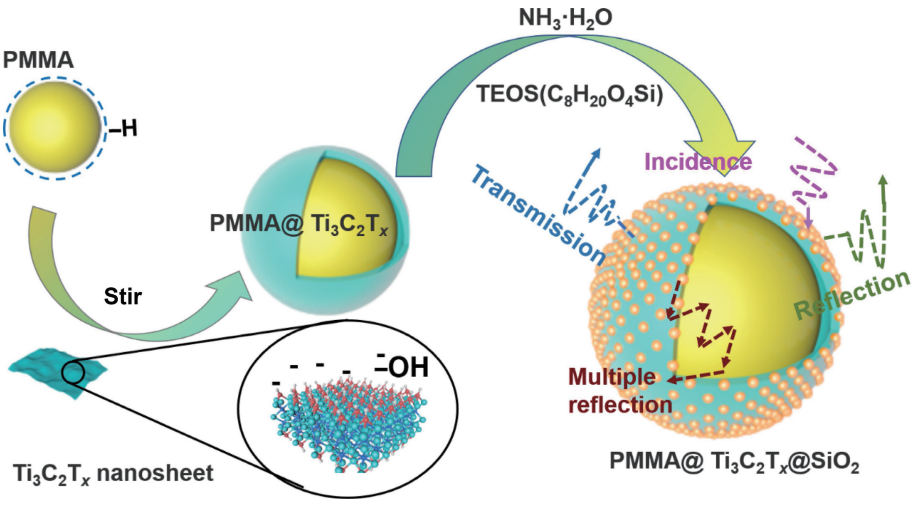

Figure 1 Illustration of the preparation method of the PMMA@$Ti_3C_2T_x$@SiO_2 composites.

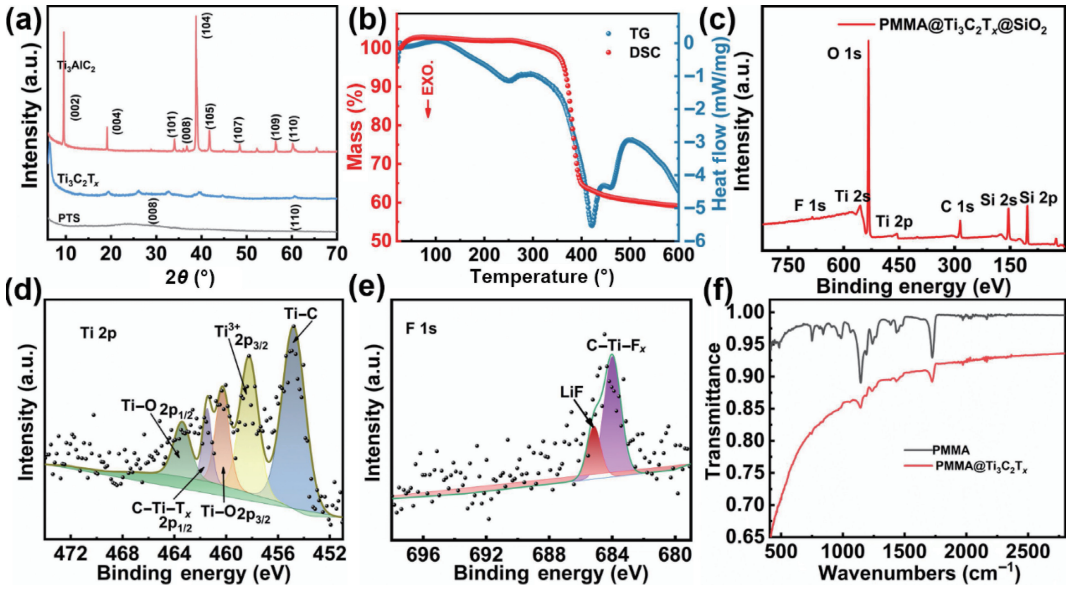

Figure 2 Analysis of sample composition: (a) XRD patterns of Ti_3AlC_2, $Ti_3C_2T_x$ and PMMA@$Ti_3C_2T_x$@SiO_2 composites, (b) TG-DSC image of PMMA@$Ti_3C_2T_x$@SiO_2 composites, (c) XPS survey spectrum of PMMA@$Ti_3C_2T_x$@SiO_2 composites (PTS-3), (d) Ti 2p and (e) F 1s high-resolution XPS spectra of PMMA@$Ti_3C_2T_x$@SiO_2 composites (PTS-3), and (f) infrared spectrum of PMMA and PMMA@$Ti_3C_2T_x$, respectively.

Figure 2(a) illustrates the XRD patterns of the raw materials (Ti_3AlC_2), $Ti_3C_2T_x$ and the resulting PMMA@$Ti_3C_2T_x$@SiO_2 composites with sandwich-like core–shell structure. It can be seen that a distinct broad diffraction peak at approximately 22° is observed, which can be ascribed to the presence of amorphous SiO_2 [28]. Additionally, two diffraction peaks are evident at 29.3° and 60.8° of PTS, corresponding to the (008) and (110) crystal planes of $Ti_3C_2T_x$ nanosheets, respectively [29]. However, the diffraction peak belonging to the (002) crystal plane of $Ti_3C_2T_x$ nanosheets is not observed, which aligns with the findings from our prior research. We have previously discussed that the bending and folding of the nanosheets lead to an expansion of the interplanar space of the (002) plane, resulting in uneven interplanar space [30].

Figure 2(b) shows the thermogravimetric-differential scanning calorimetry (TG-DSC) analysis of PMMA@$Ti_3C_2T_x$@SiO_2 composites heated from room temperature to 600 °C at a heating rate of 20 °C/min under oxygen atmosphere. As observed, the TG curve exhibits a sharp drop around 400 °C, corresponding to the decomposition of PMMA microspheres [31]. Furthermore, the DSC curve displays a prominent exothermic peak in the range of 300 to 400 °C, compensating for the heat absorbed during the PMMA decomposition. Beyond 400 °C, additionally, a noticeable increase in mass can be observed. This increase is attributed to the oxidation process of $Ti_3C_2T_x$, which is strongly influenced by the presence of oxygen and water molecules, and is known to accelerate at higher temperatures [32, 33]. Consequently, this leads to a clear mass gain beyond 400 °C.

The X-ray photoelectron spectroscopy was used to further analyze elemental compositions and valence states of the PMMA@$Ti_3C_2T_x$@SiO_2 composites. The wide-scan survey spectrum (Fig. 2(c)) confirms the presence of Ti, C, F, O, and Si elements in the composites, providing evidence of the combination between PMMA, $Ti_3C_2T_x$ and SiO_2. Further analysis under high-resolution XPS reveals detailed chemical states of the elements. In the Ti 2p spectrum (Fig. 2(d)), five peaks at 454.9, 457.9, 459.7, 461.5 and 463.9 eV, corresponding to Ti–C, Ti^{3+} $2p_{3/2}$, Ti–O $2p_{3/2}$, C–Ti–T_x $2p_{1/2}$ and Ti–O $2p_{1/2}$, respectively [34]. The high-resolution XPS spectrum of F 1s (Fig. 2(e)) show two deconvolution peaks at 685.05 and 683.98 eV, corresponding to LiF and C–Ti–F_x, respectively [27]. The presence of C–Ti–F_x is beneficial for enhancing the effective EWA performance of the composites, as it induces a strong dipolar polarization effect, leading to significant microwave attenuation performance [35]. The presence of LiF is a negligible trace, introduced during the etching process of the Ti_3AlC_2 precursor and subsequently

removed through multiple washes. The above results indicate that PMMA@$Ti_3C_2T_x$@SiO_2 composites have been successfully prepared and possess strong antioxidant properties below 200 °C.

The morphologies of the PMMA, PMMA@$Ti_3C_2T_x$, and PMMA@$Ti_3C_2T_x$@SiO_2 composites were characterized using SEM and TEM. SEM micrograph in Fig. 3(a) reveals the presence of PMMA microspheres with uniform size around 1.8 μm. In Fig. 3(b), the microstructure of PMMA@$Ti_3C_2T_x$ shows $Ti_3C_2T_x$ nanosheets forming a wrinkled film-like structure, wrapping around the surface of PMMA microspheres. The interaction between PMMA and $Ti_3C_2T_x$ is attributed to hydrogen bonding facilitated by the –OH functional groups presented on the $Ti_3C_2T_x$ nanosheets [36, 37]. The effect of hydrogen bonding was further confirmed by infrared spectrum (Fig. 2(f)), where the hydroxyl stretching vibration peak of PMMA@$Ti_3C_2T_x$ composite shifts to 1233 cm^{-1} compared to pure PMMA (1240 cm^{-1}). Additionally, the numerous defects on the surface of $Ti_3C_2T_x$ nanosheets provide active sites for the preparation of SiO_2-coated PMMA@$Ti_3C_2T_x$ composites. As a result, SiO_2 is evenly anchored on the surface of PMMA@$Ti_3C_2T_x$, forming a dense oxide coating (Figs. 3(c)–3(f)). The dielectric parameters of PMMA@$Ti_3C_2T_x$@SiO_2 composites can be tuned by adjusting the amount of SiO_2 production.

Furthermore, the microstructural composition of PMMA@$Ti_3C_2T_x$@SiO_2 composites was further investigated by TEM. Figures 3(g) and 3(h) display the TEM images of PMMA@$Ti_3C_2T_x$@SiO_2 composites, illustrating their distinct sandwich-like core–shell structure. Moreover, Figs. 3(i)–3(l) show the surface of PMMA@$Ti_3C_2T_x$@SiO_2 containing numerous dense SiO_2 particles.

In order to investigate the elemental distribution of the obtained sample, PTS-3 was selected for energy dispersive X-ray spectroscopy (EDS) mapping analysis at the position indicated in Fig. 3(k). Figure 3(l) illustrates the EDS mapping results, showing consistent distribution patterns of Si and O elements, further confirming the presence of SiO_2. Additionally, the Ti element is uniformly distributed but in lower abundance, which can be attributed to the relatively low incorporation of $Ti_3C_2T_x$ nanosheets. Notably, the C element is concentrated in the center and exhibits a round shape, consistent with the shape of PMMA. While the peripheral distribution of C element is less dense and correlates with the distribution of Ti element, corresponding to the $Ti_3C_2T_x$ nanosheets. This finding affirms the successful preparation of PMMA@$Ti_3C_2T_x$@SiO_2 composites with sandwich-like core–shell structure. Moreover, the SiO_2 layer serves as a protective barrier, mitigating the issue of facile oxidation of $Ti_3C_2T_x$ nanosheets, thus extending its potential applications to relatively high temperature environments.

3.2 Electromagnetic parameters and EWA performance

The complex permittivity ($\varepsilon_r = \varepsilon' - j\varepsilon''$) and permeability ($\mu_r = \mu' - j\mu''$) are crucial electromagnetic parameters used to evaluate the effective EWA performance of the samples [38]. Since the resultant composites exhibit no magnetism properties, their EWA performance mainly relies on the complex dielectric loss. It is widely recognized that the real part ε' represents the storage capacity of electromagnetic wave energy [39], while the imaginary part ε'' represents the dissipation ability [19, 40]. Similarly, μ' and μ'' represent the real and imaginary part of permeability, respectively. Therefore, the electromagnetic parameters of both PMMA@$Ti_3C_2T_x$ and PMMA@$Ti_3C_2T_x$@SiO_2 composites were calculated using the transmission line principle at varying thicknesses ranging from 1 to 5 mm.

The EM parameters of PMMA@$Ti_3C_2T_x$ composites were calculated and are shown in Fig. 4(a). To intuitively evaluate the effective EWA performance of the samples, the reflection loss (RL) is computed based on the transmission line theory according to the following formula [41–45]

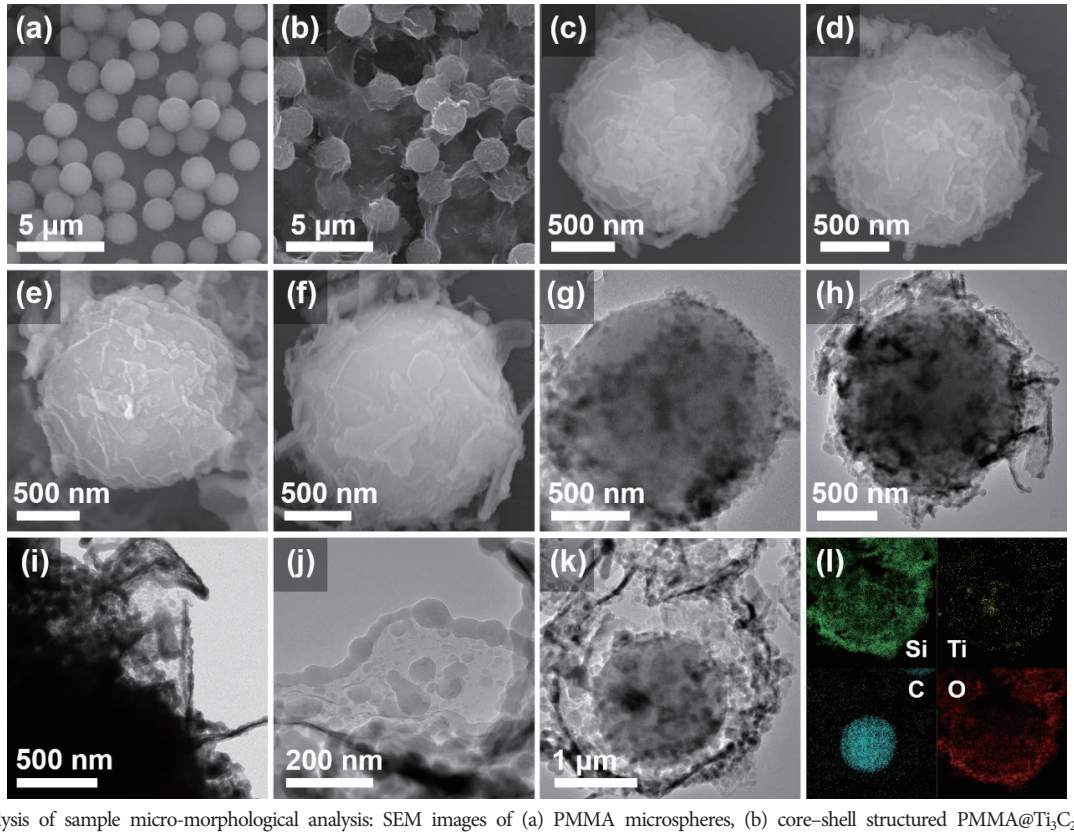

Figure 3 Analysis of sample micro-morphological analysis: SEM images of (a) PMMA microspheres, (b) core–shell structured PMMA@$Ti_3C_2T_x$, (c)–(f) the PMMA@$Ti_3C_2T_x$@SiO_2 composites with different amount of TEOS (TEOS = 2, 3, 4, and 5 mL, respectively). (g)–(k) TEM images of PMMA@$Ti_3C_2T_x$@SiO_2 composites. (i) Elemental TEM-EDS mapping analysis of PMMA@$Ti_3C_2T_x$@SiO_2 composites.

$$RL = 20\lg\left|\frac{Z_{in}-Z_0}{Z_{in}+Z_0}\right| \quad (1)$$

$$Z = Z_{in}/Z_0 = \sqrt{\frac{\mu_r}{\varepsilon_r}}\tanh\left[j\left(\frac{2\pi fd}{c}\right)\sqrt{\mu_r\varepsilon_r}\right] \quad (2)$$

$$\alpha = \frac{\sqrt{2}\pi f}{c}\times\sqrt{(\mu''\varepsilon''-\mu'\varepsilon')+\sqrt{(\mu''\varepsilon''-\mu'\varepsilon')^2+(\mu'\varepsilon''+\mu''\varepsilon')^2}} \quad (3)$$

where Z_{in}, Z_0, f, d and c represent normalized input impedance of the absorber, the impedance of free space, the frequency of the EM wave, the thickness of the absorber, and the velocity of light in free space, respectively [46, 47].

As can been seen that the PMMA@$Ti_3C_2T_x$ composites exhibit a high imaginary part ε'' and attenuation constant, which can be attributed to the ultra-high conductivity of $Ti_3C_2T_x$ nanosheets. This high conductivity, in turn, leads to low skin depth and causes impedance mismatch (Fig. 4(c)) [48]. Therefore, when incident electromagnetic wave encounters the surface of PMMA@$Ti_3C_2T_x$, a substantial portion of the waves will be reflected, resulting in poor EWA performance of PMMA@$Ti_3C_2T_x$, as illustrated in Fig. 4(b).

Upon the introduction of SiO_2, the complex permittivity of PMMA@$Ti_3C_2T_x$@SiO_2 composites experiences a significant decrease compared to PMMA@$Ti_3C_2T_x$ composites. The real part values vary as follows: 19.24 to 18.49, 21.83 to 21.14, 22.14 to 22.05, and 30.68 to 30.38 for PMMA@$Ti_3C_2T_x$@SiO_2 composites with different TEOS additions, respectively (Fig. 5(a)). The imaginary part values are within the range of 7.22 to 6.91, 5.89 to 5.61, 6.74 to 5.76, and 6.22 to 5.85, respectively. As mentioned above, the relatively higher imaginary part of PTS-1 leads to the reflection of incident electromagnetic waves, resulting in inferior wave absorption performance. Conversely, an excessive SiO_2 coating in PTS-4 leads to a lower imaginary part, which fails to effectively deplete the incident electromagnetic wave, and also results in poor EWA performance.

PTS-2 and PTS-3 exhibit suitable complex permittivity achieved by an appropriate amount of SiO_2, enabling efficient absorption of electromagnetic waves. These composites not only allow the waves to enter the absorber but also effectively consume electromagnetic wave energy. Similar conclusions can also be drawn from the tanδ_ε (Fig. 5(c)) and α (Fig. 5(d)) results of the samples. Additionally, as seen in Fig. 5(b), the ε'' curves of PTS-2 and PTS-3 samples display evident Debye dielectric relaxation peaks, which contribute to enhancing the EWA performance [23, 28]. In summary, an appropriate SiO_2 coating on the surface of PMMA@$Ti_3C_2T_x$ composites can not only adjust the dielectric parameters of PMMA@$Ti_3C_2T_x$@SiO_2 composites, but also impart an optical fiber-like structure that facilitates the induction of electromagnetic waves into the material for loss.

To visually illustrate the relationship between absorption performance, frequency and thickness, the three-dimensional (3D) RL diagram of different samples was simulated and the results are presented in Fig. 6. The PMMA@$Ti_3C_2T_x$@SiO_2 composites exhibit superior electromagnetic wave absorption performance compared to PMMA@$Ti_3C_2T_x$ composites. Specifically, the RL values of PMMA@$Ti_3C_2T_x$@SiO_2 composites show an enhanced trend with the gradual increase SiO_2 content, followed by a weakening effect at higher SiO_2 content. This indicates that the presence of SiO_2 significantly influences the EWA performance, the mechanism will be discussed in the subsequent section.

Surprisingly, the PTS-3 sample exhibits the strongest reflection loss, reaching up to −58.08 dB at an ultra-thin thickness of 1.9 mm, corresponding to an EAB of 2.88 GHz. Moreover, within the thickness range of 1–5 mm, the EAB of the PTS-3 sample (Fig. 7(c)) extends up to 14.76 GHz, mainly attributed to the suitable impedance match in 2–18 GHz frequency range (Fig. 7(b)). In comparison, PMMA@$Ti_3C_2T_x$, with relatively high conductivity exhibits inferior absorption performance due to the limited surface skin effect, preventing effective electromagnetic wave absorption. Obviously, the SiO_2 coating with excellent microwave transmittance, not only induces electromagnetic wave to penetrate the absorbers' interior but also tunes the dielectric parameters to enhance absorption performance, effectively achieving a "two birds with one stone" effect.

3.3 Mechanisms for the enhanced EWA properties

The loss mechanisms of absorbers are intricately related to electromagnetic parameters of materials. It is well known that excellent electromagnetic wave absorption materials must satisfy

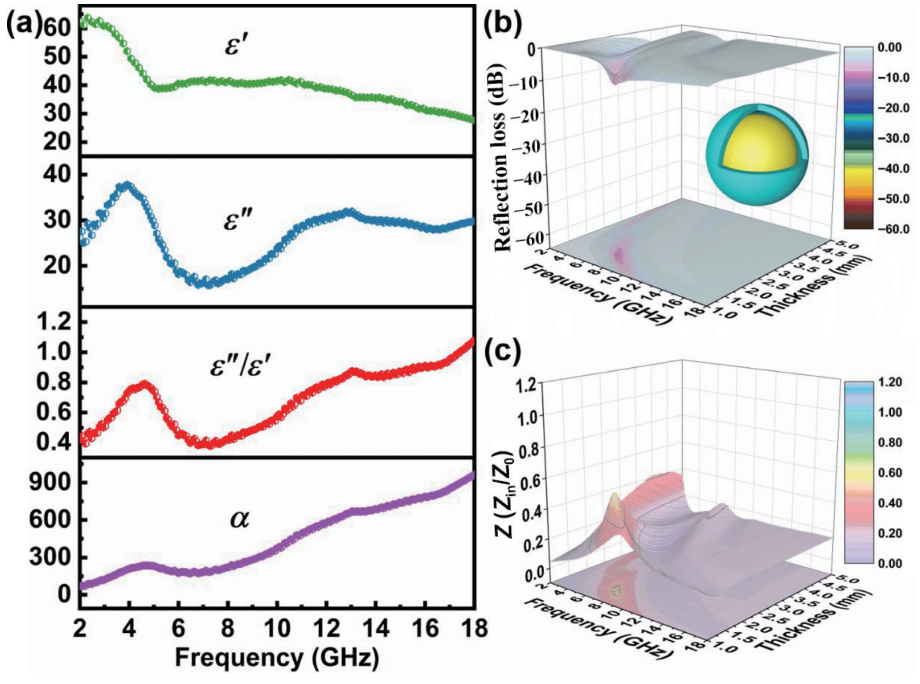

Figure 4 Absorption performance of PMMA@$Ti_3C_2T_x$: (a) electromagnetic parameters of PMMA@$Ti_3C_2T_x$, (b) 3D reflection loss curves and contour map, and (c) impedance match of PMMA@$Ti_3C_2T_x$

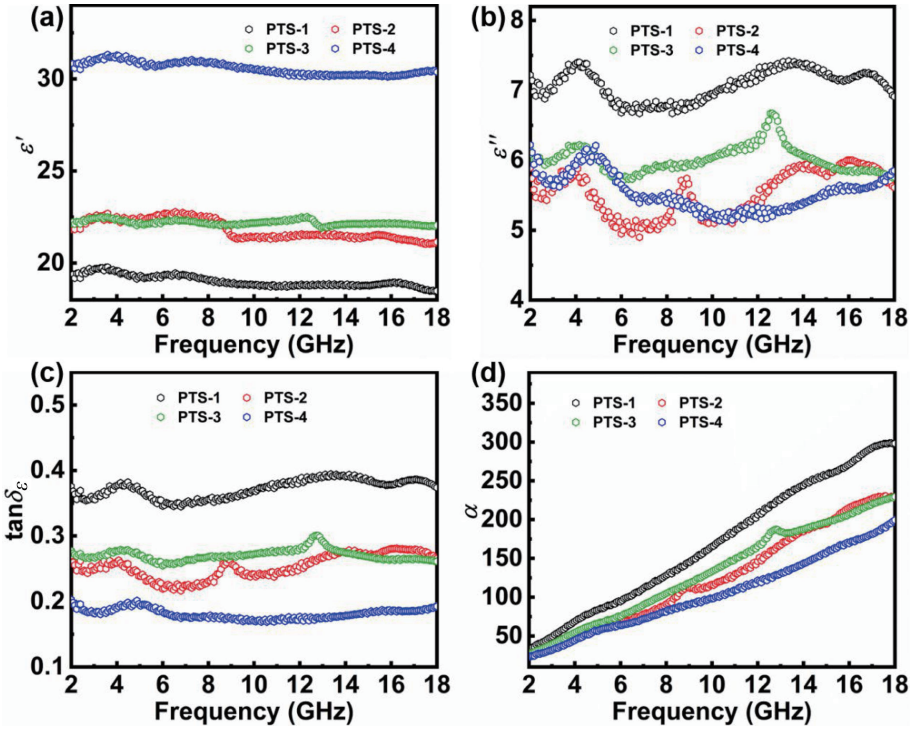

Figure 5 The connection between electromagnetic parameters (a) ε' , (b) ε'', (c) tanδ_ε, and (d) α and frequency of PMMA@$Ti_3C_2T_x$@SiO_2 composites with different amount of TEOS (TEOS = 2, 3, 4, and 5 mL, respectively).

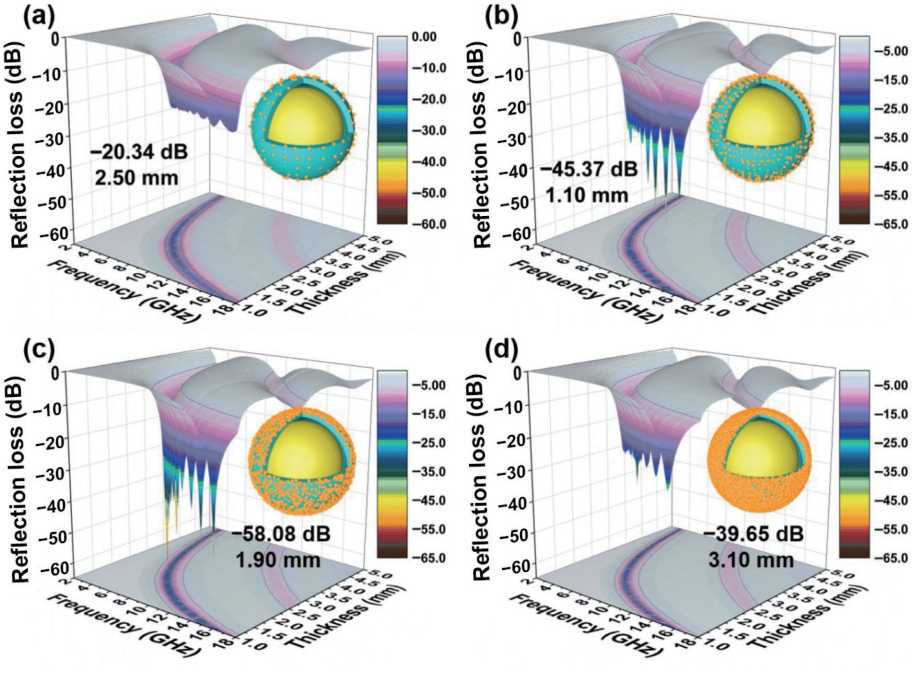

Figure 6 3D reflection loss curves and contour map of PMMA@$Ti_3C_2T_x$@SiO_2 composites with different amount of TEOS (TEOS = 2 (a), 3 (b), 4 (c), and 5 (d) mL, respectively)

two conditions. Firstly, they should achieve impedance match, wherein the surface impedance of the material closely matches that of free space [49, 50]. This ensures that more electromagnetic waves can be incident into the absorber for subsequent attenuation. The second condition is the attenuation characteristic [29, 51], which necessitates sufficient polarization and conductance loss to effectively attenuate the incident electromagnetic wave.

Electromagnetic wave absorption requires the absorber to possess impedance match characteristics [52]. Impedance match refers to the surface impedance of the absorber being close to the impedance of free space ($Z = Z_{in}/Z_0 = 1$) [53]. When EM waves are incident on the absorber' surface, three processes occur: reflection, absorption, and transmission [54]. By regulating the impedance matching, the goal of reducing reflection and increasing absorption of incident EM waves can be achieved. Calculations have shown that the optimal impedance match value of an absorption material should be between 0.8 to 1.2 [55].

The impedance match values of PMMA@$Ti_3C_2T_x$ are considerably lower than 0.8 (Fig. 4(c)), indicating that it does not meet the requirement of optimal impedance match. Similarly, the 3D impedance match contour maps of PMMA@$Ti_3C_2T_x$@SiO_2 composites are shown in Fig. 8. Among them, PTS-1 exhibits impedance match values lower than 0.8, while PTS-4 has

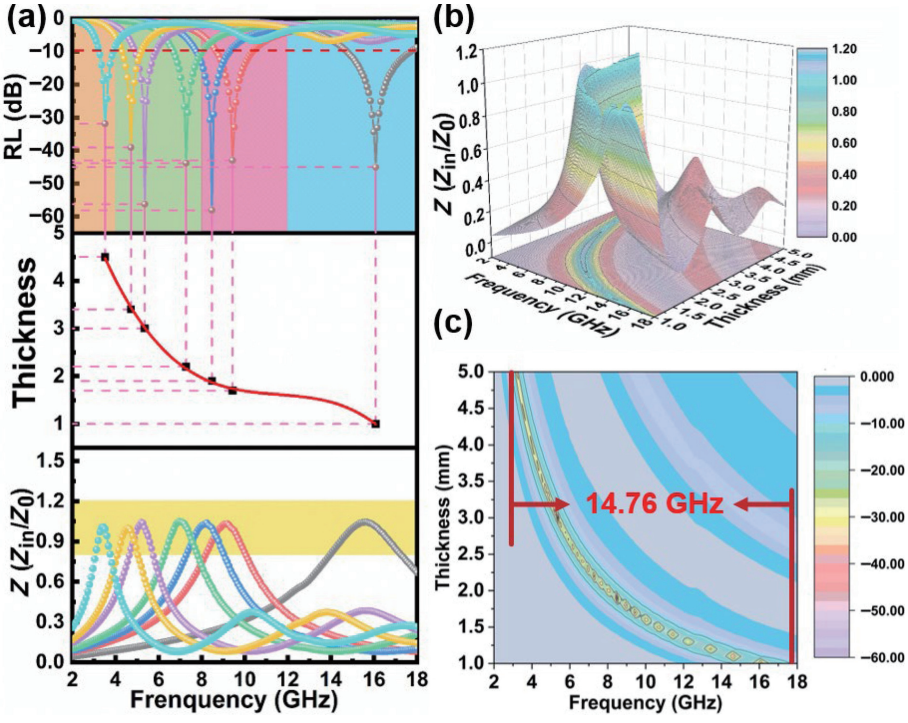

Figure 7 Absorption performance of PTS-3: (a) the EWA properties and the corresponding thickness simulation, (b) the $Z = Z_{in}/Z_0$ and (c) reflection loss contour image of PTS-3

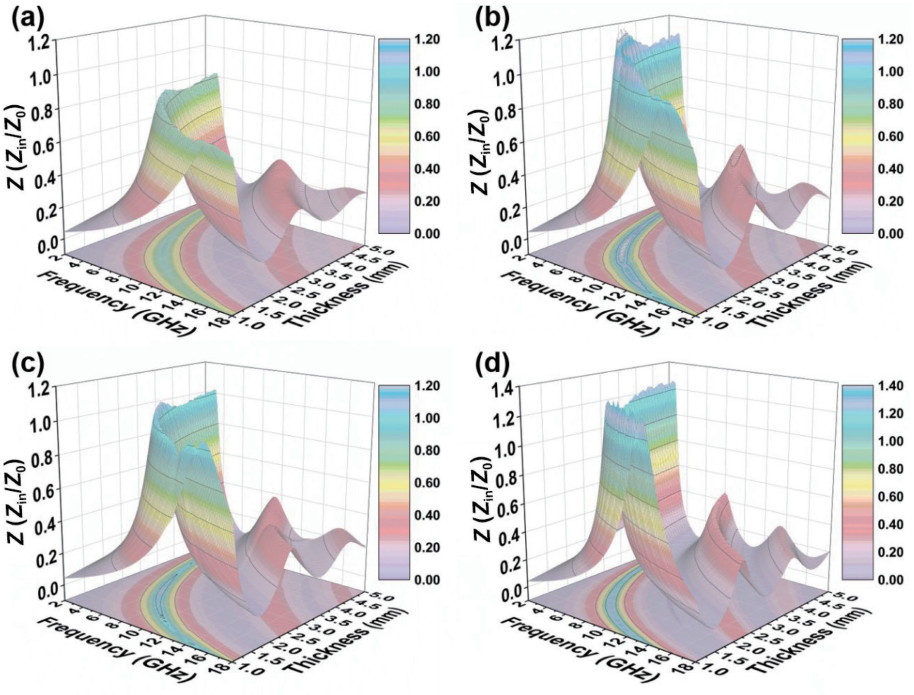

Figure 8 3D impedance match curves and contour map of PMMA@$Ti_3C_2T_x$@SiO_2 composites with different amount of TEOS (TEOS = 2 (a), 3 (b), 4 (c), and 5 mL (d), respectively).

impedance match values higher than 1.2 across most of the frequency range. Both situations lead to the reflection of most incident electromagnetic waves and result in poor microwave absorption performance.

Comparatively, PTS-2 and PTS-3 samples show impedance match values between 0.8 and 1.2, covering a broader frequency range. Furthermore, the impedance match values of PTS-3 are close to 1, indicating a good impedance match compared to other samples. This favorable impedance match in PTS-3 is attributed to its sandwich-like core–shell structure, the electrical conductivity provided by $Ti_3C_2T_x$ nanosheets, and the appropriate content of SiO_2. In summary, the impedance match is closely related to electromagnetic parameters, which are determined by the composition and structure of the absorber. Achieving an optimal impedance match is crucial for enhancing the electromagnetic wave absorption performance of the materials.

The wave absorption performance of a material depends on the synergistic effects of multiple attenuation loss characteristics, which involve appropriate attenuation constants, conductive networks, and multiple polarizations [56]. Previous studies have shown that materials with an attenuation constant in the range of 25–350 exhibit excellent absorption properties [29, 51, 57]. The attenuation constant of PMMA@$Ti_3C_2T_x$ sample exceeds 350 (Fig. 4(a)), indicating that a significant portion of incident

electromagnetic waves will be reflected. On the other hand, the electromagnetic parameters of PMMA@$Ti_3C_2T_x$@SiO_2 composites show noticeable adjustability due to the presence of SiO_2 coating, enabling them to possess a suitable attenuation constant and to achieve enhanced wave absorption properties.

Moreover, a 3D conductive network is established by numerous defects and functional groups on the surface of $Ti_3C_2T_x$ nanosheets, acting as carriers that effectively attenuate electromagnetic wave energy [58]. This conductive network further contributes to the improved wave absorption performance of the PMMA@$Ti_3C_2T_x$@SiO_2 composites. The presence of SiO_2 coating and the conductive network work in synergy to create an absorber with enhanced absorption characteristics, ensuring that incident electromagnetic waves are efficiently attenuated and absorbed.

Polarization loss is an important mechanism of electromagnetic wave attenuation. The PMMA@$Ti_3C_2T_x$@SiO_2 composites, with their sandwich-like core–shell structure, provide a large number of interfaces, leading to interfacial polarization effects in the constantly changing EM field [59]. Moreover, the $Ti_3C_2T_x$ nanosheets possess abundant inherent defects and terminating functional groups that act as polarization center. Under high-frequency EM fields, these defects induce polarization and dipolar polarization.

Furthermore, the SiO_2 coating not only improves impedance matching but also causes multiple internal reflection of the electromagnetic wave. This prolongs the propagation path of electromagnetic waves within the composite [60], leading to enhanced polarization loss. The combined effect of interfacial polarization, defect-induced polarization, dipolar polarization, and multiple internal reflections contributes to the overall polarization loss of the PMMA@$Ti_3C_2T_x$@SiO_2 composites, making them efficient absorbers of electromagnetic waves.

In order to further investigate the mechanism behind the enhanced EWA properties, we employed off-axis electron holography to explore the polarization behavior and charge distribution within the PMMA@$Ti_3C_2T_x$@SiO_2 composites under alternating electromagnetic fields. Off-axis electron holography is a powerful electron microscopy-based technique that provides nanometer-scale resolution for characterizing electrostatic potentials and charge density distributions [61]. In the TEM images of PMMA@$Ti_3C_2T_x$@SiO_2 composites (Figs. 9(a) and 9(b)), we observe a rich phase boundary with uneven distribution around it (Figs. 9(d)–9(i)). This leads to the generation of numerous dipole moments when subject to electromagnetic fields. The sandwich-like core–shell structure of composites, with a significant difference in the inherent electromagnetic parameters of SiO_2 and $Ti_3C_2T_x$ nanosheets, results in the formation of multiple interfacial polarization, which contribute to the polarization loss of the electromagnetic wave [62–64].

Moreover, the excitation of electromagnetic energy causes electrons to migrate along the $Ti_3C_2T_x$/SiO_2 optical fiber-like structure and pass through barriers such as stacking sites, contact sites and atomic defects. This generates a capacitance-like structure that effectively attenuates electromagnetic waves [65]. Under the action of alternating electromagnetic field, electron flow occurs from the SiO_2 coating to the inner $Ti_3C_2T_x$ nanosheets, creating a space charge region on the thin surface with significantly different electromagnetic parameters. This facilitates accumulation of charge in this region [66].

Furthermore, the existence of a dipole moments in the PMMA@$Ti_3C_2T_x$@SiO_2 composites allows for the conversion of

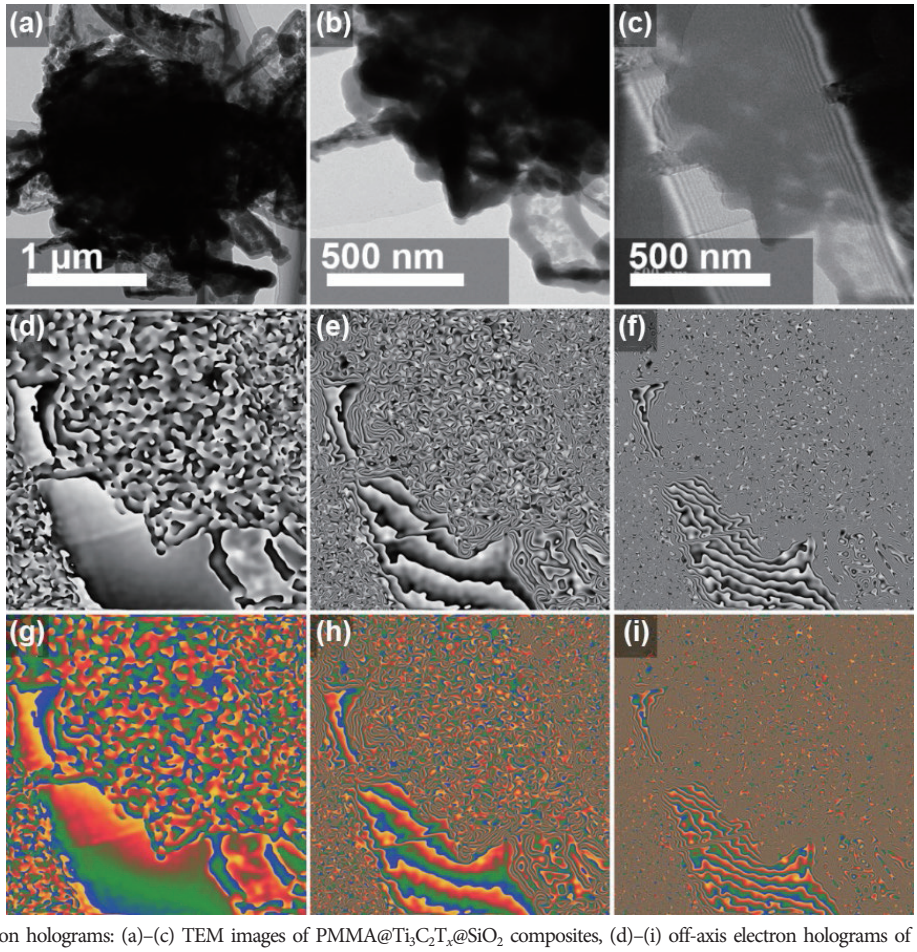

Figure 9 Off-axis electron holograms: (a)–(c) TEM images of PMMA@$Ti_3C_2T_x$@SiO_2 composites, (d)–(i) off-axis electron holograms of c images under different electromagnetic amplification signals.

electromagnetic wave energy into thermal energy through the polarization behavior of the accumulated charge at the interface [7]. These combined mechanisms contribute to the enhanced EWA properties of the PMMA@$Ti_3C_2T_x$@SiO_2 composites.

Summarily, the absorption mechanisms of PMMA@$Ti_3C_2T_x$@SiO_2 composites are illustrated in Fig. 10. Firstly, the high conductivity of $Ti_3C_2T_x$ nanosheets, with numerous defects and terminal groups, contribute to the conductivity loss in PMMA@$Ti_3C_2T_x$@SiO_2 composites, leading to improved EWA performance. Secondly, the presence of heterogeneous interfaces ($Ti_3C_2T_x$/SiO_2 and $Ti_3C_2T_x$/PMMA interfaces) in the composites results in interfacial polarization when subjected to alternating electromagnetic fields, which further enhances the EWA capabilities. Additionally, PMMA@$Ti_3C_2T_x$@SiO_2 composites exhibit abundant dipoles on $Ti_3C_2T_x$ nanosheets, generating a significant dipolar polarization effect. Moreover, electromagnetic waves experience multiple reflections and scattering at the interface, contributing to the attenuation of the incident waves. In summary, the EWA performance of PMMA@$Ti_3C_2T_x$@SiO_2 composites relies on a synergistic combination of various loss mechanisms, including conductivity loss, interfacial polarization loss, dipolar polarization loss and multiple reflections, all of which work together to effectively attenuate electromagnetic waves.

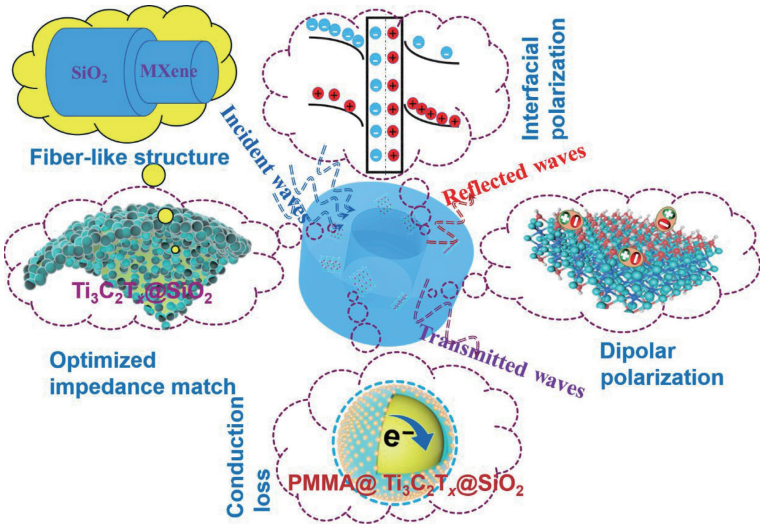

Figure 10 Electromagnetic wave absorption mechanisms of PMMA@$Ti_3C_2T_x$@SiO_2 composites.

4 Conclusions

In this study, PMMA@$Ti_3C_2T_x$@SiO_2 composites were successfully prepared using hydrogen bonding and sol-gel method. The well-designed sandwich-like core–shell structure and 3D $Ti_3C_2T_x$@SiO_2 optical fiber-like structure result in excellent impedance match and strong attenuation efficiency. Therefore, the PMMA@$Ti_3C_2T_x$@SiO_2 composites exhibit outstanding absorption performance, benefiting from the synergistic effect of interface loss and dipolar loss due to the presence of SiO_2 coating. The material exhibits a minimum reflection loss value of −58.08 dB at an ultra-thin thickness of 1.9 mm, with an effective absorption bandwidth of 2.88 GHz. Moreover, the effective absorption bandwidth covers 14.76 GHz in the adjustable thickness range of 1–5 mm. This finding show case the potential of high-performance $Ti_3C_2T_x$-based composites for electromagnetic wave absorption applications.

Acknowledgements

This work was supported by the National Natural Science Foundation of China (No. U2004177), Henan Province Key Research Project for Higher Education Institutions (No. 23B430017), the Outstanding Youth Fund of Henan Province (No. 212300410081), and the Science and Technology Innovation Talents in Universities of Henan Province (No. 22HASTIT001). B. B. F. also acknowledged the financial support from the Research and Entrepreneurship Start-up Projects for Overseas Returned Talents.

Funding note: Open Access funding enabled and organized by Projekt DEAL

References

[1] Song, Q.; Ye, F.; Kong, L.; Shen, Q. L.; Han, L. Y.; Feng, L.; Yu, G. J.; Pan, Y. N.; Li, H. J. Graphene and MXene nanomaterials: Toward high-performance electromagnetic wave absorption in gigahertz band range. *Adv. Funct. Mater.* **2020**, *30*, 2000475.

[2] Cao, M. S.; Cai, Y. Z.; He, P.; Shu, J. C.; Cao, W. Q.; Yuan, J. 2D MXenes: Electromagnetic property for microwave absorption and electromagnetic interference shielding. *Chem. Eng. J.* **2019**, *359*, 1265–1302.

[3] Lu, Y. H.; Zhang, S. L.; He, M. Y.; Wei, L.; Chen, Y.; Liu, R. N. 3D cross-linked graphene or/and MXene based nanomaterials for electromagnetic wave absorbing and shielding. *Carbon* **2021**, *178*, 413–435.

[4] Zhang, Z. W.; Cai, Z. H.; Zhang, Y.; Peng, Y. L.; Wang, Z. Y.; Xia, L.; Ma, S. P.; Yin, Z. Z.; Wang, R. F.; Cao, Y. S. et al. The recent progress of MXene-Based microwave absorption materials. *Carbon* **2021**, *174*, 484–499.

[5] Zhang, Y.; Huang, Y.; Zhang, T. F.; Chang, H. C.; Xiao, P. S.; Chen, H. H.; Huang, Z. Y.; Chen, Y. S. Broadband and tunable high-performance microwave absorption of an ultralight and highly compressible graphene foam. *Adv. Mater.* **2015**, *27*, 2049–2053.

[6] Li, X. L.; Yin, X. W.; Song, C. Q.; Han, M. K.; Xu, H. L.; Duan, W. Y.; Cheng, L. F.; Zhang, L. T. Self-assembly core–shell graphene-bridged hollow MXenes spheres 3D foam with ultrahigh specific EM absorption performance. *Adv. Funct. Mater.* **2018**, *28*, 1803938.

[7] Li, Y.; Meng, F. B.; Mei, Y.; Wang, H. G.; Guo, Y. F.; Wang, Y.; Peng, F. X.; Huang, F.; Zhou, Z. W. Electrospun generation of $Ti_3C_2T_x$ MXene@graphene oxide hybrid aerogel microspheres for tunable high-performance microwave absorption. *Chem. Eng. J.* **2020**, *391*, 123512.

[8] Deng, B. W.; Liu, Z. C.; Pan, F.; Xiang, Z.; Zhang, X.; Lu, W. Electrostatically self-assembled two-dimensional magnetized MXene/hollow Fe_3O_4 nanoparticle hybrids with high electromagnetic absorption performance and improved impendence matching. *J. Mater. Chem. A* **2021**, *9*, 3500–3510.

[9] Li, X.; You, W. B.; Wang, L.; Liu, J. W.; Wu, Z. C.; Pei, K.; Li, Y. S.; Che, R. C. Self-assembly-magnetized MXene avoid dual-agglomeration with enhanced interfaces for strong microwave absorption through a tunable electromagnetic property. *ACS Appl. Mater. Interfaces* **2019**, *11*, 44536–44544.

[10] Li, X.; You, W. B.; Xu, C. Y.; Wang, L.; Yang, L. T.; Li, Y. S.; Che, R. C. 3D seed-germination-like MXene with *in situ* growing CNTs/Ni heterojunction for enhanced microwave absorption via polarization and magnetization. *Nano-Micro Lett.* **2021**, *13*, 157.

[11] Zhang, Y. L.; Ruan, K. P.; Zhou, K.; Gu, J. W. Controlled distributed $Ti_3C_2T_x$ hollow microspheres on thermally conductive polyimide composite films for excellent electromagnetic interference shielding. *Adv. Mater.* **2023**, *35*, 2211642.

[12] Liang, L. Y.; Han, G. J.; Li, Y.; Zhao, B.; Zhou, B.; Feng, Y. Z.; Ma, J. M.; Wang, Y. M.; Zhang, R.; Liu, C. T. Promising $Ti_3C_2T_x$ MXene/Ni chain hybrid with excellent electromagnetic wave absorption and shielding capacity. *ACS Appl. Mater. Interfaces* **2019**, *11*, 25399–25409.

[13] Cui, Y. H.; Yang, K.; Wang, J. Q.; Shah, T.; Zhang, Q. Y.; Zhang, B. L. Preparation of pleated RGO/MXene/Fe_3O_4 microsphere and its absorption properties for electromagnetic wave. *Carbon* **2021**, *172*, 1–14.

[14] Liu, P. B.; Zhang, G. Z.; Xu, H. X.; Cheng, S. C.; Huang, Y.; Ouyang, B.; Qian, Y. T.; Zhang, R. X.; Che, R. C. Synergistic dielectric-magnetic enhancement via phase-evolution engineering and dynamic magnetic resonance. *Adv. Funct. Mater.* **2023**, *33*, 2211298.

[15] Du, H.; Zhang, Q. P.; Zhao, B.; Marken, F.; Gao, Q. C.; Lu, H. X.; Guan, L.; Wang, H. L.; Shao, G.; Xu, H. L. et al. Novel hierarchical structure of $MoS_2/TiO_2/Ti_3C_2T_x$ composites for dramatically enhanced electromagnetic absorbing properties. *J. Adv. Ceram.* **2021**, *10*, 1042–1051.

[16] Fan, B. B.; Ansar, M. T.; Chen, Q. Q.; Wei, F. C.; Du, H.; Ouyang, B.; Kan, E. J.; Chen, Y. Q.; Zhao, B.; Zhang, R. Microwave-assisted hydrothermal synthesis of 2D/2D $MoS_2/Ti_3C_2T_x$ heterostructure for enhanced microwave absorbing performance. *J. Alloys Compd.* **2022**, *923*, 166253.

[17] Li, X. L.; Yin, X. W.; Han, M. K.; Song, C. Q.; Xu, H. L.; Hou, Z. X.; Zhang, L. T.; Cheng, L. F. Ti_3C_2 MXenes modified with *in situ* grown carbon nanotubes for enhanced electromagnetic wave absorption properties. *J. Mater. Chem. C* **2017**, *5*, 4068–4074.

[18] Huang, M. Q.; Wang, L.; Pei, K.; You, W. B.; Yu, X. F.; Wu, Z. C.; Che, R. C. Multidimension-controllable synthesis of MOF-derived Co@N-doped carbon composite with magnetic-dielectric synergy toward strong microwave absorption. *Small* **2020**, *16*, 2000158.

[19] Wang, J. Q.; Liu, L.; Jiao, S. L.; Ma, K. J.; Lv, J.; Yang, J. J. Hierarchical carbon fiber@MXene@MoS_2 core–sheath synergistic microstructure for tunable and efficient microwave absorption. *Adv. Funct. Mater.* **2020**, *30*, 2002595.

[20] Wei, C. H.; He, M. K.; Li, M. Q.; Ma, X.; Dang, W. L.; Liu, P. B.; Gu, J. W. Hollow Co/NC@MnO_2 polyhedrons with enhanced synergistic effect for high-efficiency microwave absorption. *Mater. Today Phys.* **2023**, *36*, 101142.

[21] Shen, Z. J.; Yang, H. L.; Xiong, Z. Q.; Xie, Y.; Liu, C. B. Hollow core–shell CoNi@C and CoNi@NC composites as high-performance microwave absorbers. *J. Alloys Compd.* **2021**, *871*, 159574.

[22] Li, Z. J.; Lin, H.; Xie, Y. X.; Zhao, L. B.; Guo, Y. Y.; Cheng, T. T.; Ling, H. L.; Meng, A. L.; Li, S. X.; Zhang, M. Monodispersed Co@C nanoparticles anchored on reclaimed carbon black toward high-performance electromagnetic wave absorption. *J. Mater. Sci. Technol.* **2022**, *124*, 182–192.

[23] Zhang, S.; Zhang, F.; Xie, Y. Y.; Niu, H. H.; Li, Y. Y.; Wang, H. L.; Zhang, R.; Li, H. X.; Wang, X. H.; Fan, B. B. Ultrathin CoNi@$Ti_3C_2T_x$ composites with sandwich structures for efficient microwave absorption. *Ceram. Int.* **2022**, *48*, 33751–33762.

[24] Chen, Q. Q.; Fan, B. B.; Zhang, Q. P.; Wang, S.; Cui, W.; Jia, Y. C.; Xu, S. K.; Zhao, B.; Zhang, R. Design of 3D lightweight $Ti_3C_2T_x$ MXene porous film with graded holes for efficient electromagnetic interference shielding performance. *Ceram. Int.* **2022**, *48*, 14578–14586.

[25] Jiang, Z. Y.; Gao, Y. J.; Pan, Z. H.; Zhang, M. M.; Guo, J. H.; Zhang, J. W.; Gong, C. H. Pomegranate-like ATO/SiO_2 microspheres for efficient microwave absorption in wide temperature spectrum. *J. Mater. Sci. Technol.* **2024**, *174*, 195–203.

[26] Liang, Q. Q.; Wang, L.; Qi, X. S.; Peng, Q.; Gong, X.; Chen, Y. L.; Xie, R.; Zhong, W. Hierarchical engineering of CoNi@Air@C/SiO_2@polypyrrole multicomponent nanocubes to improve the dielectric loss capability and magnetic-dielectric synergy. *J. Mater. Sci. Technol.* **2023**, *147*, 37–46.

[27] Niu, H. H.; Tu, X. Y.; Zhang, S.; Li, Y. Y.; Wang, H. L.; Shao, G.; Zhang, R.; Li, H. X.; Zhao, B.; Fan, B. B. Engineered core–shell SiO_2@$Ti_3C_2T_x$ composites: Towards ultra-thin electromagnetic wave absorption materials. *Chem. Eng. J.* **2022**, *446*, 137260.

[28] Jiang, X. W.; Niu, H. H.; Li, J. L.; Li, M. R.; Ma, C.; Zhang, R.; Wang, H. L.; Lu, H. X.; Xu, H. L.; Fan, B. B. Construction of core–shell structured SiO_2@MoS_2 nanospheres for broadband electromagnetic wave absorption. *Appl. Surf. Sci.* **2023**, *628*, 157355.

[29] Wang, Y.; Gao, X.; Zhang, L. J.; Wu, X. M.; Wang, Q. G.; Luo, C. Y.; Wu, G. L. Synthesis of Ti_3C_2/Fe_3O_4/PANI hierarchical architecture composite as an efficient wide-band electromagnetic absorber. *Appl. Surf. Sci.* **2019**, *480*, 830–838.

[30] Niu, H. H.; Jiang, X. W.; Xia, Y. D.; Wang, H. L.; Zhang, R.; Li, H. X.; Fan, B. B.; Zhou, Y. C. Construction of *hydrangea*-like core–shell SiO_2@$Ti_3C_2T_x$@CoNi microspheres for tunable electromagnetic wave absorbers. *J. Adv. Ceram.* **2023**, *12*, 711–723.

[31] Nikolaidis, A. K.; Achilias, D. S. Thermal degradation kinetics and viscoelastic behavior of poly(methyl methacrylate)/organomodified montmorillonite nanocomposites prepared via *in situ* bulk radical polymerization. *Polymers* **2018**, *10*, 491.

[32] Liu, N.; Li, Q. Q.; Wan, H. J.; Chang, L. B.; Wang, H.; Fang, J. H.; Ding, T. P.; Wen, Q. Y.; Zhou, L. J.; Xiao, X. High-temperature stability in air of $Ti_3C_2T_x$ MXene-based composite with extracted bentonite. *Nat. Commun.* **2022**, *13*, 5551.

[33] Huang, S. H.; Mochalin, V. N. Hydrolysis of 2D transition-metal carbides (MXenes) in colloidal solutions. *Inorg. Chem.* **2019**, *58*, 1958–1966.

[34] He, P.; Cao, M. S.; Shu, J. C.; Cai, Y. Z.; Wang, X. X.; Zhao, Q. L.; Yuan, J. Atomic layer tailoring titanium carbide MXene to tune transport and polarization for utilization of electromagnetic energy beyond solar and chemical energy. *ACS Appl. Mater. Interfaces* **2019**, *11*, 12535–12543.

[35] Shahzad, F.; Alhabeb, M.; Hatter, C. B.; Anasori, B.; Man Hong, S.; Koo, C. M.; Gogotsi, Y. Electromagnetic interference shielding with 2D transition metal carbides (MXenes). *Science* **2016**, *353*, 1137–1140.

[36] Wang, X. H.; Bao, S.; Hu, F. Y.; Shang, S. Y.; Chen, Y. Q.; Zhao, N.; Zhang, R.; Zhao, B.; Fan, B. B. The effect of honeycomb pore size on the electromagnetic interference shielding performance of multifunctional 3D honeycomb-like Ag/$Ti_3C_2T_x$ hybrid structures. *Ceram. Int.* **2022**, *48*, 16892–16900.

[37] Li, Q.; Jiao, Q. Z.; Li, H. J.; Yan, Y.; Lu, C. X.; Shen, X. R.; Gu, T. T.; Zhou, W.; Zhao, Y.; Li, H. S. et al. Constructing layered double hydroxide derived heterogeneous $Ti_3C_2T_x$@S-MCoP (M = Ni, Mn,

Zn) with S-vacancies to boost sodium storage performance. *J. Mater. Chem. A* **2022**, *10*, 21690–21700.
[38] Xu, H. X.; He, Z. Z.; Li, Y. R.; Wang, Y. R.; Zhang, Z. W.; Dai, X. Q.; Xiong, Z. M.; Geng, W. C.; Liu, P. B. Porous magnetic carbon spheres with adjustable magnetic-composition and synergistic effect for lightweight microwave absorption. *Carbon* **2023**, *213*, 118290.
[39] Zhao, Y. P.; Zuo, X. Q.; Guo, Y.; Huang, H.; Zhang, H.; Wang, T.; Wen, N. X.; Chen, H.; Cong, T. Z.; Muhammad, J. et al. Structural engineering of hierarchical aerogels comprised of multi-dimensional gradient carbon nanoarchitectures for highly efficient microwave absorption. *Nano-Micro Lett.* **2021**, *13*, 144.
[40] Wu, Z. C.; Pei, K.; Xing, L. S.; Yu, X. F.; You, W. B.; Che, R. C. Enhanced microwave absorption performance from magnetic coupling of magnetic nanoparticles suspended within hierarchically tubular composite. *Adv. Funct. Mater.* **2019**, *29*, 1901448.
[41] Han, Y. X.; He, M. K.; Hu, J. W.; Liu, P. B.; Liu, Z. W.; Ma, Z. L.; Ju, W. B.; Gu, J. W. Hierarchical design of FeCo-based microchains for enhanced microwave absorption in C band. *Nano Res.* **2023**, *16*, 1773–1778.
[42] Guo, Y. Q.; Ruan, K. P.; Wang, G. S.; Gu, J. W. Advances and mechanisms in polymer composites toward thermal conduction and electromagnetic wave absorption. *Sci. Bull.* **2023**, *68*, 1195–1212.
[43] Zuo, X. Q.; Zhang, H.; Zhou, C.; Zhao, Y. P.; Huang, H.; Wen, N. X.; Sun, C.; Fan, Z.; Pan, L. J. Hierarchical and porous structures of carbon nanotubes-anchored MOF derivatives bridged by carbon nanocoils as lightweight and broadband microwave absorbers. *Small* **2023**, *19*, 2301992.
[44] Xiao, J. X.; Qi, X. S.; Gong, X.; Peng, Q.; Chen, Y. L.; Xie, R.; Zhong, W. Defect and interface engineering in core@shell structure hollow carbon@MoS_2 nanocomposites for boosted microwave absorption performance. *Nano Res.* **2022**, *15*, 7778–7787.
[45] Wei, C. H.; Shi, L. Z.; Li, M. Q.; He, M. K.; Li, M. J.; Jing, X. R.; Liu, P. B.; Gu, J. W. Hollow engineering of sandwich NC@Co/NC@MnO_2 composites toward strong wideband electromagnetic wave attenuation. *J. Mater. Sci. Technol.*, in press, https://doi.org/10.1016/j.jmst.2023.08.020.
[46] Liu, J. W.; Che, R. C.; Chen, H. J.; Zhang, F.; Xia, F.; Wu, Q. S.; Wang, M. Microwave absorption enhancement of multifunctional composite microspheres with spinel Fe_3O_4 cores and anatase TiO_2 shells. *Small* **2012**, *8*, 1214–1221.
[47] You, H. H.; Zhang, L.; Jiang, Y. Z.; Shao, T. Y.; Li, M.; Gong, J. L. Bubble-supported engineering of hierarchical $CuCo_2S_4$ hollow spheres for enhanced electrochemical performance. *J. Mater. Chem. A* **2018**, *6*, 5265–5270.
[48] Guo, R.; Fan, Y. C.; Wang, L. J.; Jiang, W. Core-rim structured carbide MXene/SiO_2 nanoplates as an ultrathin microwave absorber. *Carbon* **2020**, *169*, 214–224.
[49] Gu, W. H.; Ong, S. J. H.; Shen, Y. H.; Guo, W. Y.; Fang, Y. T.; Ji, G. B.; Xu, Z. J. A lightweight, elastic, and thermally insulating stealth foam with high infrared-radar compatibility. *Adv. Sci. (Weinh.)* **2022**, *9*, 2204165.
[50] Huang, Y. Q.; Yong, J.; Song, W. L.; Wen, B.; Fang, X. Y.; Cao, M. S. Microwave absorbing materials: Solutions for real functions under ideal conditions of microwave absorption. *Chin. Phys. Lett.* **2010**, *27*, 027702.
[51] Ge, C. Q.; Wang, L. Y.; Liu, G.; Wang, T. Enhanced electromagnetic properties of carbon nanotubes and SiO_2-coated carbonyl iron microwave absorber. *J. Alloys Compd.* **2018**, *767*, 173–180.
[52] Liu, P. B.; Gao, S.; Zhang, G. Z.; Huang, Y.; You, W. B.; Che, R. C. Hollow engineering to Co@N-doped carbon nanocages via synergistic protecting-etching strategy for ultrahigh microwave absorption. *Adv. Funct. Mater.* **2021**, *31*, 2102812.
[53] Han, M. K.; Yin, X. W.; Kong, L.; Li, M.; Duan, W. Y.; Zhang, L. T.; Cheng, L. F. Graphene-wrapped ZnO hollow spheres with enhanced electromagnetic wave absorption properties. *J. Mater. Chem. A* **2014**, *2*, 16403–16409.
[54] He, G. H.; Duan, Y. P.; Pang, H. F. Microwave absorption of crystalline Fe/MnO@C nanocapsules embedded in amorphous carbon. *Nano-Micro Lett.* **2020**, *12*, 57.
[55] Hu, F. Y.; Zhang, F.; Wang, X. H.; Li, Y. Y.; Wang, H. L.; Zhang, R.; Li, H. X.; Fan, B. B. Ultrabroad band microwave absorption from hierarchical $MoO_3/TiO_2/Mo_2TiC_2T_x$ hybrids via annealing treatment. *J. Adv. Ceram.* **2022**, *11*, 1466–1478.
[56] Xiao, J. X.; Qi, X. S.; Gong, X.; Peng, Q.; Chen, Y. L.; Xie, R.; Zhong, W. Tunable and improved microwave absorption of flower-like core@shell MFe_2O_4@MoS_2 (M = Mn, Ni and Zn) nanocomposites by defect and interface engineering. *J. Mater. Sci. Technol.* **2023**, *139*, 137–146.
[57] Shu, R. W.; Wan, Z. L.; Zhang, J. B.; Wu, Y.; Liu, Y.; Shi, J. J.; Zheng, M. D. Facile design of three-dimensional nitrogen-doped reduced graphene oxide/multi-walled carbon nanotube composite foams as lightweight and highly efficient microwave absorbers. *ACS Appl. Mater. Interfaces* **2020**, *12*, 4689–4698.
[58] Qiu, X.; Wang, L. X.; Zhu, H. L.; Guan, Y. K.; Zhang, Q. T. Lightweight and efficient microwave absorbing materials based on walnut shell-derived nano-porous carbon. *Nanoscale* **2017**, *9*, 7408–7418.
[59] Peng, H.; He, M.; Zhou, Y. M.; Song, Z. P.; Wang, Y. J.; Feng, S. J.; Chen, X.; Zhang, X. A.; Chen, H. Low-temperature carbonized biomimetic cellulose nanofiber/MXene composite membrane with excellent microwave absorption performance and tunable absorption bands. *Chem. Eng. J.* **2022**, *433*, 133269.
[60] Li, Y.; Liu, X. F.; Nie, X. Y.; Yang, W. W.; Wang, Y. D.; Yu, R. H.; Shui, J. L. Multifunctional organic-inorganic hybrid aerogel for self-cleaning, heat-insulating, and highly efficient microwave absorbing material. *Adv. Funct. Mater.* **2019**, *29*, 1807624.
[61] McCartney, M. R.; Dunin-Borkowski, R. E.; Smith, D. J. Quantitative measurement of nanoscale electrostatic potentials and charges using off-axis electron holography: Developments and opportunities. *Ultramicroscopy* **2019**, *203*, 105–118.
[62] Hu, F. Y.; Wang, X. H.; Bao, S.; Song, L. M.; Zhang, S.; Niu, H. H.; Fan, B. B.; Zhang, R.; Li, H. X. Tailoring electromagnetic responses of delaminated $Mo_2TiC_2T_x$ MXene through the decoration of Ni particles of different morphologies. *Chem. Eng. J.* **2022**, *440*, 135855.
[63] Zhang, H.; Zhao, Y. P.; Zuo, X. Q.; Huang, H.; Sun, C.; Fan, Z.; Pan, L. J. Construction of chiral-magnetic-dielectric trinity composites for efficient microwave absorption with low filling ratio and thin thickness. *Chem. Eng. J.* **2023**, *467*, 143414.
[64] Liu, P. B.; Wang, Y.; Zhang, G. Z.; Huang, Y.; Zhang, R. X.; Liu, X. H.; Zhang, X. F.; Che, R. C. Hierarchical engineering of double-shelled nanotubes toward hetero-interfaces induced polarization and microscale magnetic interaction. *Adv. Funct. Mater.* **2022**, *32*, 2202588.
[65] Meng, R.; Zhang, T.; Jiao, P. Z.; Zhang, M. F.; Huang, X. X.; Xia, L.; Zhong, B.; Zhao, H.; Wang, H. T.; Wen, G. W. Facile fabrication of SiC/Fe_xO_y embellished graphite layers with enhanced electromagnetic wave absorption. *J. Alloys Compd.* **2019**, *798*, 386–393.
[66] Wang, L.; Li, X.; Li, Q. Q.; Yu, X. F.; Zhao, Y. H.; Zhang, J.; Wang, M.; Che, R. C. Oriented polarization tuning broadband absorption from flexible hierarchical ZnO arrays vertically supported on carbon cloth. *Small* **2019**, *15*, 1900900.